ACS OMEGA

http://pubs.acs.org/journal/acsodf

Article

Extrusion-Based Bioprinting of Multilayered Nanocellulose Constructs for Cell Cultivation Using *In Situ* Freezing and Preprint $CaCl_2$ Cross-Linking

Anum Rasheed,* Latifeh Azizi, Paula Turkki, Marika Janka, Vesa P. Hytönen, and Sampo Tuukkanen*

Cite This: https://dx.doi.org/10.1021/acsomega.0c05036

Read Online

ACCESS | Metrics & More | Article Recommendations | Supporting Information

ABSTRACT: Extrusion-based bioprinting with a preprint cross-linking agent and an *in situ* cooling stage provides a versatile method for the fabrication of 3D structures for cell culture. We added varying amounts of calcium chloride as a precross-linker into native nanofibrillated cellulose (NFC) hydrogel prior to 3D bioprinting to fabricate structurally stable multilayered constructs without the need for a separate cross-linking bath. To further enhance their stability, we bioprinted the multilayered structures onto an *in situ* temperature-controlled printing stage at 25, 0, and −10 °C. The extruded and subsequently freeze-dried volumetric constructs maintained their structures after being immersed into a cell culture medium. The ability to maintain the shape after immersion in cell media is an essential feature for the fabrication of stem cell-based artificial organs. We studied the viability and distribution of mouse embryonic fibroblast cells into the hydrogels using luminescence technique and confocal microscopy. Adding $CaCl_2$ increased the stability of the multilayered nanocellulose structures, making them suitable for culturing cells inside the 3D hydrogel environment. Lower stage temperature considerably improved the structural stability of the 3D printed structures, however, had no effect on cell viability.

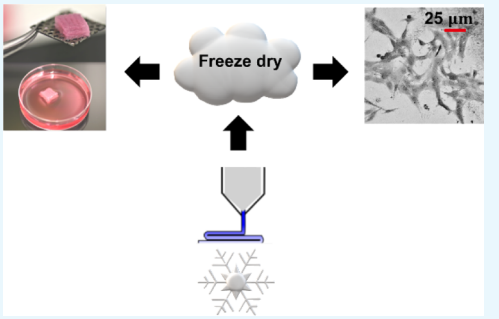

1. INTRODUCTION

With the growing concerns over ethical issues surrounding animal-based testing, scientists are inclined toward mimicking human organs in laboratories using stem cell-based methods.[1−4] This has led to a boom in organ-on-chip applications and additive manufacturing of structures from natural hydrogels with infused live cells.[5−8] As mammalian cells need a soft and aqueous environment, it is challenging to fabricate cell-compatible volumetric structures (at least 10 × 10 × 10 mm^3) *via* 3D printing.[9,10] Extracellular matrix properties required for cell attachment and shear thinning properties required for the fabrication of multilayered constructs through additive printing are not compatible with each other, making bioprinting more challenging.

For biomedical applications involving *in vitro* cell culture, 3D volumetric constructs are able to mimic the actual living cell environment better than 2D.[11−16] Nanofibrillated cellulose (NFC) is structurally similar to the extracellular matrix, providing a good support for 3D-culturing of cells.[17−20] Bioprinting involves printing of either hydrogels or cell-laden inks to fabricate computer-aided designs such as organs, tissues, vessels, *etc.* for various applications such as patient-specific organ printing and tissue engineering.[21] Bioprinting can be characterized into three groups: (1) inkjet, (2) laser, or (3) extrusion-based.[22] In the inkjet bioprinters, hydrogel beads loaded with cell aggregates are used as the prime building blocks of the structures but it lacks the precision for droplet placement. The absorbing layer expands into a bubble when it is vaporized by the laser and bursts into tiny droplets containing cells. These droplets are then forced toward the substrate.[23] However, laser-based 3D bioprinting is a costly and time-consuming process which limits the choice of bioinks to be used.[24]

In extrusion-based printing, hydrogels in the gel state are used as the printing material. Extrusion-based bioprinting allows individual cells or cell aggregates to be suspended in biopolymer gel-like nanocellulose. High viscosity bioinks can be printed using extrusion-based bioprinting with high cell density. Success in bioprinting depends on a number of parameters such as printability, biocompatibility, mechanical and structural properties, degradation of byproducts, and biomimicry ability of the biomaterial used for printing.[12] Extrusion-based printability further depends on five device-controlled parameters, namely, dispensing nozzle diameter, pneumatic pressure, flow rate of the dispensing material, temperature of the hydrogel, and writing speed.[25]

Received: October 15, 2020
Accepted: December 11, 2020

Extrusion-based bioprinting can be used to fabricate bioprinted organs, which will not only decrease the dependency on organ donation but also provide a promising alternative to animal testing. Current research regarding bioprinted constructs use combination of different types of cellulose or/and alginate, which are cross-linked with calcium chloride to form 3D structures.[26−32] In previous studies, the structures were printed inside a calcium chloride bath for postprinting cross-linkage,[27−31] few drops of calcium chloride were added during the printing process,[33] or a combination of both.[26] Rees *et al.* applied $CaCl_2$ solution on the printed structure during the printing process.[33] Postprinting cross-linking or aerosol spray causes the multilayered structures to lose their structural integrity quickly when exposed to moisture or during cell culturing as the 3D structures are cross-linked at the surfaces only. The low percentage of dry-matter content in hydrogels makes it challenging to prevent the multilayered structure from collapsing.[34] Layer-by-layer stacking is challenging when the overhanging filaments collapse, affecting the overall structural stability. The resolution and the desired pore size of the printed 3D structures are also compromised.[35] Because of poor mechanical stability of hydrogels, the multilayered complex structures fail to maintain their structure postprinting.[36] In this paper, we explore an alternative approach to fabricate structurally stable multilayered structures using ink composed of nanocellulose and calcium chloride in aqueous media. The volumetric structures are bioprinted layer-by-layer directly on top of the cooling stage to enable instantaneous freezing, greatly increasing the structural fidelity of the printed structures. To the best of our knowledge, this is the first case of investigation of the fabrication of multilayered structures using nanocellulose cross-linked with calcium chloride before extrusion-based 3D printing.

2. EXPERIMENTAL SECTION

2.1. Materials. The concentration range of $CaCl_2$ added in the NFC was taken from the literature[26−33] as the amount of $CaCl_2$ that can be added depends on cell type. Previously, the 3D prints have been either directly printed into $CaCl_2$ solution for postprinting cross-linking or *in situ* cross-linking with concentration ranging from 50 to 100 mM $CaCl_2$, as shown in Table S1. In this study, three different concentrations of $CaCl_2$ were added in NFC to find the best combination of NFC and $CaCl_2$ for producing the structurally stable scaffold without negatively affecting cell culture of mouse embryonic fibroblast (WT-MEF) cells. Three different concentrations of 19.3, 57.9, and 96.5 mM $CaCl_2$ were added into 1.15 weight percent (wt %) NFC to obtain NFC + 0.22 wt %, NFC + 0.67 wt %, and NFC + 1.08 wt % $CaCl_2$, respectively.

NFC 1.15 wt % was provided by the Department of Bioproducts and Biosystems, Aalto University, Espoo, Finland. NFC was prepared by disintegrating never-dried and fully bleached birch fibers described elsewhere.[37] $CaCl_2$ was purchased from Sigma-Aldrich.

2.2. Methods. *2.2.1. Rheology Test.* Rheology tests were performed using a discovery hybrid rheometer (HR2) with 20 mm parallel plate−plate configuration at 25 °C. Soak time of 300 s was kept constant for each sample and a solvent trap was used for each measurement to avoid drying. Amplitude sweep, frequency sweep, and flow sweep were conducted and described in detail later in the Results section. Five replicas of each sample were tested and then an average value was calculated for each sample to ensure the reliability of the test and to reduce error. An amplitude strain of 0.01−200% was applied which was used to obtain the linear region for performing frequency sweep. Frequency sweep was conducted between 0.1 and 100 Hz with a constant strain of 0.1%. Flow sweep ranging from 0.01 to 300 s^{-1} was performed to achieve the viscosity *versus* shear rate curve.

2.2.2. Bioprinter and In Situ Cold Stage. A Nordson EFD EV Series Automated Dispensing System was used to print the multilayered structures. The dispensing system consists of a stage and the dispenser having three printing heads. An Ultimus V High Precision Dispenser was connected to the printer. The stage can move in the *y* direction and the overhead dispenser attached to the robotic arm can be moved along *x* and *z* directions.

The movement is controlled *via* DispenseMotion computer software. The printer is equipped with a pneumatically driven microextruder (Nordson EFD E4). A liquid-cooled cold plate (Wakefield-Vette) provides heat sink to freeze the printed material directly on the substrate (9 cm × 9 cm glass plates). A liquid thermostat (LAUDA ECO RE 1050 SN) controls the temperature of the cold plate. The in-house bioprinter equipment has multiple nozzles, so the cooling stage can also be used for the fabrication of complex structures using multiple materials.[38,39]

The extrusion process plays a major role in the structural stability of the extruded structures.[40] For precise printing, the distance (*z*) between the nozzle tip and the printed surface needed to be approximately 0.5 mm. The hydrogel is printed directly on a substrate (glass plate) placed on the cooling plate to enable instantaneous freezing. The substrate is attached to the cold plate magnetically, *via* plastic fasteners with embedded permanent magnets. A 1 mm-thick iron plate is attached to the cold plate to provide freely adjustable positioning to the magnetic fasteners. Figure 1 shows the printing setup. The

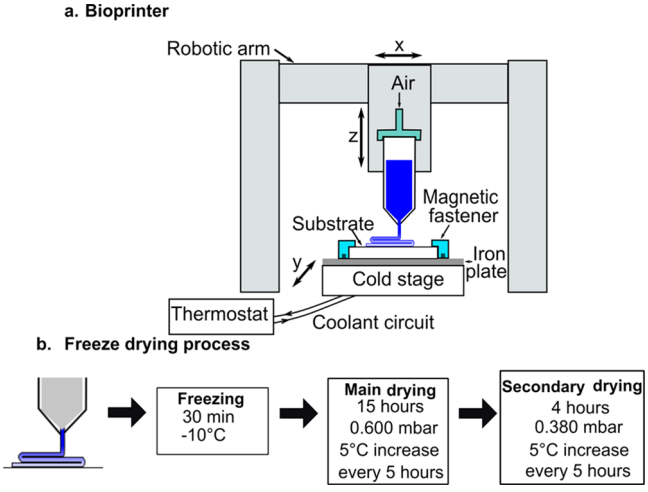

Figure 1. Diagrammatic representation of (a) extrusion-based bioprinter with an *in situ* cold stage and iron plate held by magnetic fasteners and (b) parameters used for freeze-drying.

addition of a thin iron plate did not have a significant effect on the difference between the temperature set on the cooling stage and the temperature of the glass plate on the cooling station. The difference between the cooling station setpoint temperature (−30 °C) and the temperature of the glass plate on the cooling stage was 11 °C without the iron plate and 12 °C with the iron plate. Hence, the addition of the iron plate

https://dx.doi.org/10.1021/acsomega.0c05036
ACS Omega XXXX, XXX, XXX−XXX

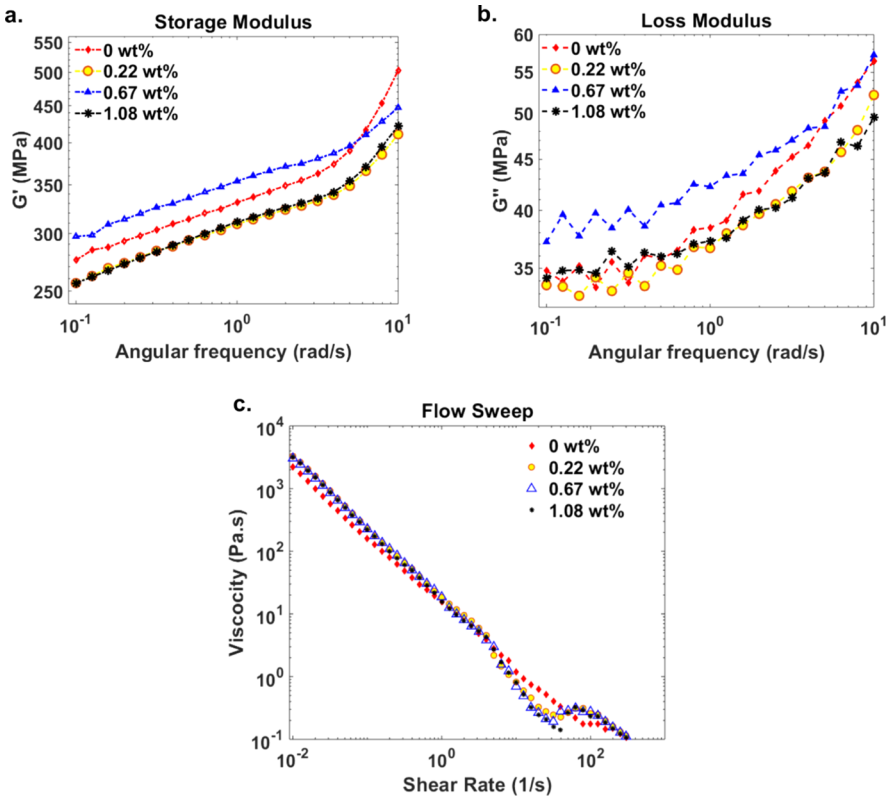

Figure 2. Graphical representation of rheological properties of the NFC with various amounts of $CaCl_2$. (a) Storage moduli, (b) loss moduli *vs* angular frequency, and (c) viscosity with respect to the shear rate for native NFC and added $CaCl_2$ amounts. For simplicity, it is referred as 0 wt % in the graphical representation to show that it is native NFC with 0, 0.22, 0.67, and 1.08 wt % added $CaCl_2$. All measurements were performed at 25 °C. Average values based on five parallel measurements are shown.

enables a secure platform for printing without adversely affecting the low temperatures of the cold plate.

All multilayered constructs were printed using a 0.15 mm Nordson stainless-steel precision tip. The pneumatic pressure used for extrusion was between 100 and 200 kPa. Percentage of relative humidity (RH) around the bioprinter was kept between 10 and 15% RH. The printing speed was 10 mm/s and the line width of each printed strand was 1 mm with a constant line spacing of 1 mm. All structures were printed at 25 °C and only the stage temperature was varied. Figure 3 shows the images of the heights and planar dimensions of all multilayered structures.

2.2.3. Freeze Dryer. To obtain stable and dry structures containing multiple layers at room temperature, freeze-drying was used after bioprinting. Printed and frozen structures were immediately transferred to the Martin Christ Epsilon 2-4 LSCplus freeze dryer to maintain structural stability. Freeze-drying, also known as lyophilization, is the process of removing water using sublimation, that is, conversion of water directly into vapor from the frozen state (ice).[41] The vapor is collected on the surface of a condenser at low temperature. The system used here has an inbuilt ice condenser capable of operating at temperatures around −88 °C and the stage temperature can be lowered down to −75 °C as silicon oil is used as the coolant. When energy is added while keeping the vacuum pressure inside the chamber below 6.11 mbar, sublimation (*i.e.,* direct conversion from liquid state to gaseous state) of water occurs. This allows gentle extraction of water from the frozen volumetric structure, resulting in a porous aerogel structure, which retains its shape at room temperature. The multilayered structures in this study were freeze-dried for 20 h and the parameters are summarized in Figure 1b.

2.2.4. Cell Culture. To test cell viability, five replicas of each sample type were applied in an ultralow attachment 96-well plate (CorningTM CostarTM Ultra-Low Attachment), which was placed on the cold stage under similar environmental conditions that were used for multilayered structures. When the plate reached the desired temperature, the hydrogels were applied by micropipetting. The samples were then freeze-dried for 20 h to form porous aerogels using the freeze-drying process mentioned above (Figure 1b). Varying amounts of samples (Table S2) were pipetted considering their shrinkage percentage during freeze-drying. As mentioned earlier, the scaffolds prepared by applying the nanocellulose hydrogel directly into the well plates are referred to as 3D structures unlike the multilayered structures, which were extruded using the bioprinter.

MEFs were maintained in high-glucose Dulbeccós modified eagle medium (DMEM) supplemented with 10% fetal bovine serum (FBS) and in a humidified 37 °C, 5% CO_2 incubator. For the cell viability assay, cells were cultured in a low-attachment 96-well plates (CorningTM CostarTM Ultra-Low Attachment plates) covered with printed NFCs and let to grow for 48 h. Cells were rinsed twice with PBS and 100 μL of Cell titer Glo (CellTiter-Glo 3D Cell Viability Assay, Promega) reagent was added. As a control, the NFCs in medium without cells were used. The luminescence signal was measured using an EnVisionTM Multilabel Plate Reader. The test was performed in five replicas and in three independent occasions.

https://dx.doi.org/10.1021/acsomega.0c05036
ACS Omega XXXX, XXX, XXX−XXX

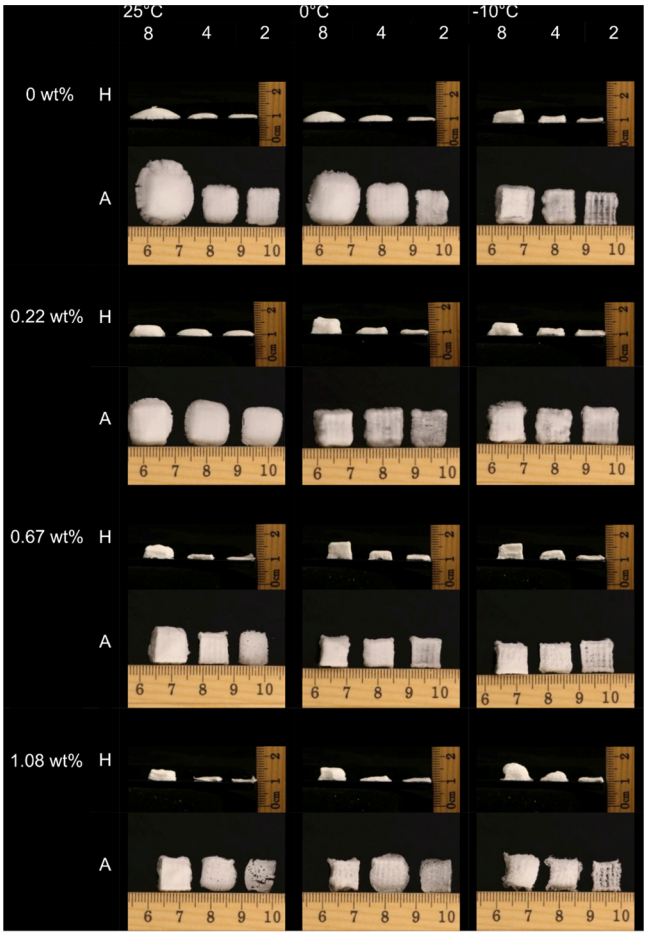

Figure 3. Images of area (A) and height (H) of 2, 4, and 8 layers (from right to left) of NFC with added amount of $CaCl_2$ printed on varying temperature of the cold stage (25, 0, and −10 °C from left to right).

For the fluorescent imaging, cells were transiently transfected with LifeAct plasmid (pCMV/pCAG-LifeAct plasmid, Ibidi) using the Neon transfection system (Thermo Fisher Scientific) according to the manufacturer's instructions. Transfected cells were cultured on glass-bottomed 96-well plates covered with different types of NFCs in triplicate. Cells were let to grow for 24 h, after which the media was changed to FluoroBright DMEM supplemented with 10% FBS. Samples were imaged with a Zeiss Cell Observer Z1 inverted microscope and LSM 780 confocal unit (Zeiss, Oberkochen, Germany) using 40×/1.14, WD 0.62 mm water immersion objective. Representative images were made with the aid of an ImageJ 3D viewer.

3. RESULTS AND DISCUSSION

3.1. Titration of Native Nanocellulose. Nanocellulose is biocompatible and nontoxic.[42−45] Nanocellulose consists of fibers with at least one dimension in nanoscale.[46] This makes NFC a suitable candidate for *in vitro* cell studies as NFC mimics the ECM which promotes the cell growth.[47−49] This together with the ability to form highly porous structures makes nanocellulose a promising candidate for the fabrication of lightweight 3D structures, films, and membrane and its properties can be easily processed in the aqueous state.[46]

Titration of native nanocellulose with 0.050 M NaOH showed that the native nanocellulose used in this study has 3.325 mmol/g of the carboxylic group present (Supporting Information). This made it possible for calcium ions to ionically cross-link with the carboxylate groups in nanocellulose, thus allowing surface manipulation of NFC.

3.2. Rheology Test Analysis. Other cellulose derivatives, such as methylcellulose, show a critical variance in the viscoelastic properties when exposed to a temperature between 40 and 50 °C because of shrinkage experience by the polymers because of hydrophobic attractions. NFC shows minor change in viscoelastic properties because of the alignment of the macromolecules to the crystalline part of the nanofibrillated structure. Hence, polymers of NFC are capable of maintaining their structure when subjected to a wide range of pH, temperatures, and ionic strength.[50] At low concentrations, NFC gel has high viscosity, which allows cells to stay suspended in the gel in the 3D shape. Moreover, NFC exhibits a change in viscosity when it is under shear stress (shear thinning). This might be because of the temporary disruption of the fibrillated network of the gel enabling the viscoelastic gel restoration within a few seconds after the removal of the shear stress force.[50] This ability of NFC to vary its viscosity with shear stress allows easy dispensing through a nozzle to print specific shapes and incorporation of cells into the gel. To study the effect of the addition of $CaCl_2$, three different mechanical tests were carried out, namely, frequency sweep, amplitude sweep, and flow sweep using Discovery-HR2. Graphs for storage modulus, loss modulus, and viscosity are shown in Figure 2a−c.

The results obtained for storage modulus G' (Figure 2a) and the loss modulus G'' (Figure 2b) *versus* angular frequency followed a similar trend for native NFC and for the hydrogels containing NFC plus the varying amounts of $CaCl_2$. Similarly, viscosity *versus* shear rate graphs for all NFC with and without $CaCl_2$ produced a similar trend (Figure 2c). Interestingly, the amount of $CaCl_2$ added in NFC was not directly proportional to the change in moduli. The addition of $CaCl_2$ lowered both the storage and loss modulus compared to native NFC. However, the highest amount of $CaCl_2$ increased both loss and storage modulus which means that the hydrogel became stiffer. All hydrogels experienced noticeable shear thinning; viscosity significantly decreased with an increase in the shear rate from 0.01 to 300 s^{-1}. Hence, all these hydrogels are suitable for extrusion printing.

3.3. Fabrication of the Multilayered Structures. The bioprinter was programmed to extrude two, four, and eight layers with areas of 100 mm^2 and a height of 2, 4, and 8 mm, respectively. In this paper, we refer to extruded volumetric structures as multilayered structures, and the pipetted structures are called 3D structures. As the structures were printed on the cooling stage, they are referred as frozen structures even for 25 °C to discriminate them from the freeze-dried structures.

We observed decreased area and increased height as the temperature of the cooling stage was decreased from 25 to −10 °C. Therefore, the cooling station was found to play a significant role in the fabrication of structurally stable volumetric constructs. Figure 1 shows the dimensions achieved by each scaffold printed on the varying cold stage temperature for each amount of $CaCl_2$ added in the native NFC.

The temperature of the cooling stage had an immense impact on the structural integrity of the multilayered structures. Lower temperature not only enabled the fabrication of structurally stable prints but also allowed the printing of

https://dx.doi.org/10.1021/acsomega.0c05036
ACS Omega XXXX, XXX, XXX−XXX

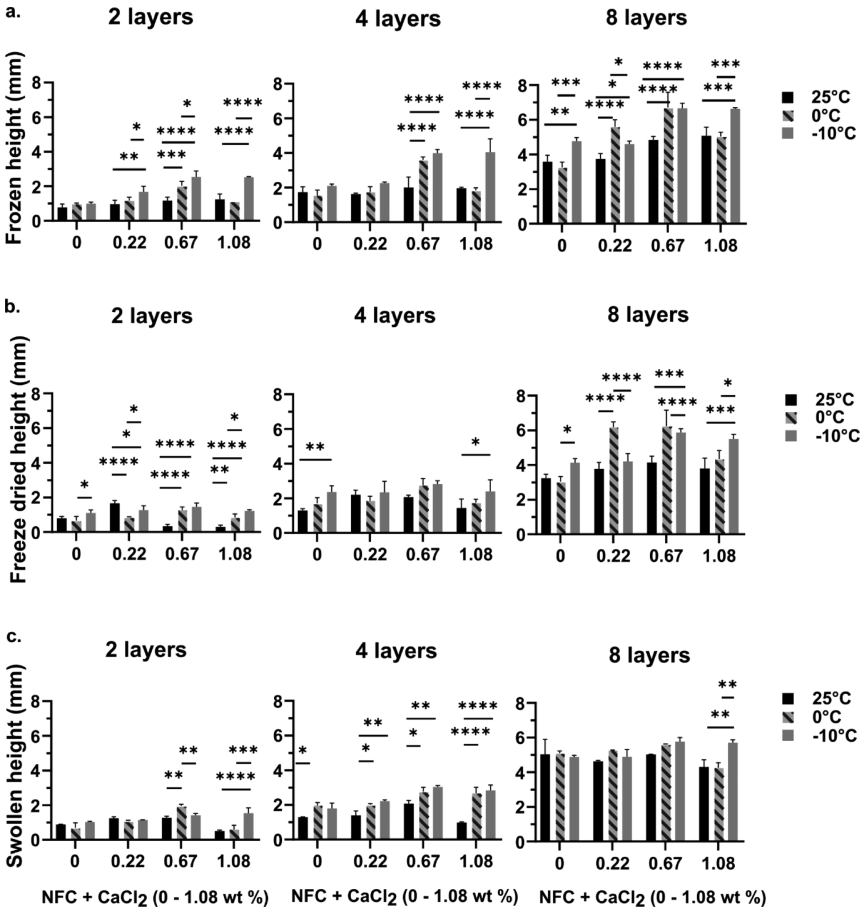

Figure 4. Effect of the cooling stage temperature and $CaCl_2$ concentration on height. Height of 2, 4, and 8 layers of (a) multilayered extruded samples on the cooling stage at three different temperatures, (b) freeze-dried samples, and (c) after swelling in cell media for 24 h. The height of the volumetric structures is measured using a vernier calliper after printing, freeze-drying, and swelling test. Two-way Anova analysis with Tukey test for p-value <0.05 is performed with three replicas and represented in a−c. Each sample type at 25 °C was taken as the reference value for the values obtained at 0 and −10 °C and the p-values were calculated in relation to the value obtain for 25 °C. 0.0332 (*P), 0.0021 (**P), 0.0002 (***P), and <0.0001 (****P).

additional layers without compromising the desired dimensions. Eight layers of NFC without any added $CaCl_2$ spread the most and therefore compromised the height reached. It was not possible to visualize the difference between the 0.22 and 0.67 $CaCl_2$ scaffolds with the naked eye. However, the addition of 1.08 wt % $CaCl_2$ made the multilayered structures fragile because of the lowest nanocellulose fiber content and high $CaCl_2$-to-nanocellulose ratio. Both the addition of $CaCl_2$ and lowering the temperature of the cooling stage helped in the fabrication of stable multilayered volumetric constructs (Figure 3). Multilayered structures containing 0.22 wt % $CaCl_2$ content which are printed at −10 °C achieved most swelling height after swelling in cell media for 24 h (Figures 4, 5 and 6). Moreover, out of all samples containing 0.22 wt % $CaCl_2$, those printed at −10 °C had the highest change in mass after swelling (Figure 6c).

For two-layered frozen structures, the maximum height was achieved with 0.67 wt % $CaCl_2$ printed at −10 °C. 1.08 wt % four-layered structures printed at −10 °C were the highest and were closely followed by 0.67 wt % (−10 °C), without any significant height difference between them. Both 0.67 wt % (0 °C) and 0.67 wt % (−10 °C) yielded the highest eight-layered frozen structures.

After freeze-drying the samples, their dimensions were measured using a vernier calliper. In general, a decrease in the overall height was observed for all the samples (Figure 4b). The highest (1.67 mm) two-layered freeze-dried structure was 0.22 wt % (25 °C) closely followed by 0.67 wt % (−10 °C) (1.46 mm). 0.67 wt % (0 and −10 °C) were the highest four-layered freeze-dried structures (2.75 and 2.82 mm, respectively). 0.67 wt % (0 °C) and 0.22 wt % (0 °C) were the highest eight-layered freeze-dried structures (6.23 and 6.17 mm) with 0.67 wt % (−10 °C) shortly falling behind (5.86 mm). Overall, not much variation in swelling height (Figure 4c) was observed and 0.67 wt % (0 and −10 °C) showed the highest structures. The change in height during freeze-drying was calculated and is described later (Figure 6a).

Figure 5 shows that 0.22 and 0.67 wt % containing scaffolds exhibit a significant reduction in area when the temperature of the cooling stage was reduced. This shows that the area of 0.22 and 0.67 wt % containing structures is the most concise and best mimic the programmed dimensions for both the frozen (Figure 5a) and freeze-dried (Figure 5b) states for all two, four, and eight layers. For frozen structures (Figure 5a), 0.22 wt % (25 °C) had the smallest area for the two-layered structures. Four-layered structures 0.22 wt % (0 °C) and 0.67 wt % (−10 °C) maintained the smallest area. The eight-layered scaffold (0.67 wt %) printed at −10 °C achieved the smallest area. This shows that the addition of $CaCl_2$ prevented the spreading of the extruded scaffolds.

https://dx.doi.org/10.1021/acsomega.0c05036
ACS Omega XXXX, XXX, XXX−XXX

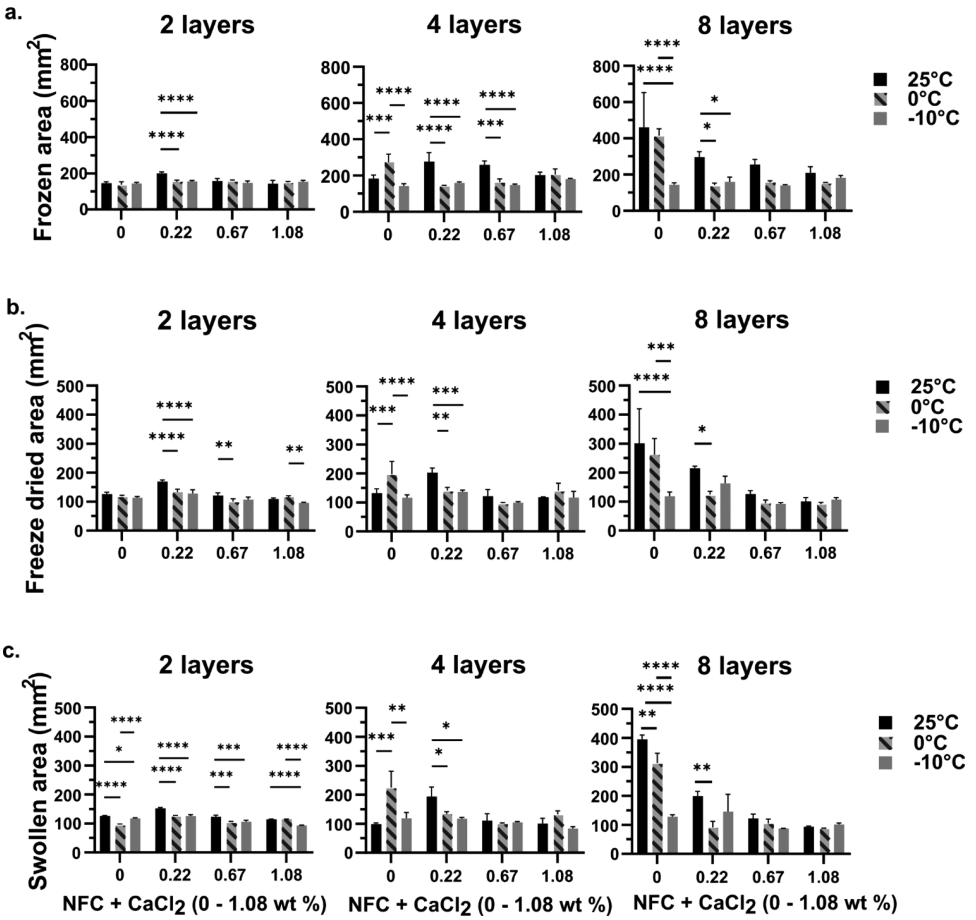

Figure 5. Effect of cooling stage temperature and $CaCl_2$ concentration on the area of the printed structures. Area of 2, 4, and 8 layers of (a) multilayered extruded samples on the cooling stage at three different temperatures, (b) freeze-dried samples, and (c) after swelling in cell media for 24 h. The area (mm^2) for all three states, that is, frozen, freeze-dried, and swollen scaffolds was calculated after measuring the length using vernier callipers. Two-way Anova analysis with Tukey test was conducted for two replicas. *P*-values <0.05 are shown on the graphs with respect to the respective sample's area of the volumetric structure printed at 25 °C. 0.0332 (*P), 0.0021 (**P), 0.0002 (***P), and <0.0001 (***P).

Like height, area of the scaffolds also reduced after freeze-drying. The smallest area for all two-, four-, and eight-layered freeze-dried structure was achieved by 0.67 wt % extruded at both 0 and −10 °C (Figure 5b). After leaving the structures to swell for 24 h, the area of all structures stayed close to that of their freeze-dried area, except for only NFC scaffolds containing 0 wt % $CaCl_2$ (Figure 5c). This shows that lower temperature of the cooling stage enables the fabrication of structurally stable multilayered structures and the addition of $CaCl_2$ in the hydrogels prior to printing enables the structures to maintain their shape during swelling. The change in the swelling area with respect to the freeze-dried area was calculated and analyzed in detail (Figure 6b).

3.4. Swelling Degree and Water Uptake. To analyze the effect of temperature at which the structures are printed on the change in height/area between freeze-dried and the swollen structures (after 24 h), the percentage of change in height, area, and the water uptake with respect to change in mass, eqs 1, 2, and 3 were used to calculate percentage of swelling degree height (SD_H), swelling degree area (SD_A), and change in mass (ΔMass).

$$SD_H(\%) = \left(\frac{H_{hydrated} - H_{dry}}{H_{dry}}\right) \times 100 \quad (1)$$

$$SD_A(\%) = \left(\frac{A_{hydrated} - A_{dry}}{A_{dry}}\right) \times 100 \quad (2)$$

In eqs 1 and 2, $H_{hydrated}$ and $A_{hydrated}$ are the swollen sample's height and area, respectively, after it is allowed to swell in the cell media for 24 h. H_{dry} and A_{dry} are the height and area of the freeze-dried structure. SD_H (%) is the percentage of the swelling degree according to the height and SD_A (%) is the percentage of the swelling degree in relation to the area of the 3D scaffolds.

Water uptake is calculated using eq 3.

$$\Delta Mass\ (\%) = \left(\frac{M_{hydrated} - M_{dry}}{M_{dry}}\right) \times 100 \quad (3)$$

where ΔMass (%) is the percentage of water uptake with respect to mass (g) and $M_{hydratyed}$ and M_{dry} are the mass (g) after immersion in cell media solution for 24 h and mass of freeze-dried structures, respectively.

Figure 6a shows that NFC + 0 wt % Ca experienced significant SD_H (%) because of the significant decrease in height with colder stage temperature. The addition of Ca did not allow spreading or collapsing of the negative SD_H (%) which shows that if the height decreased, the positive value depicts an increase in the height. The only significant trend

https://dx.doi.org/10.1021/acsomega.0c05036
ACS Omega XXXX, XXX, XXX−XXX

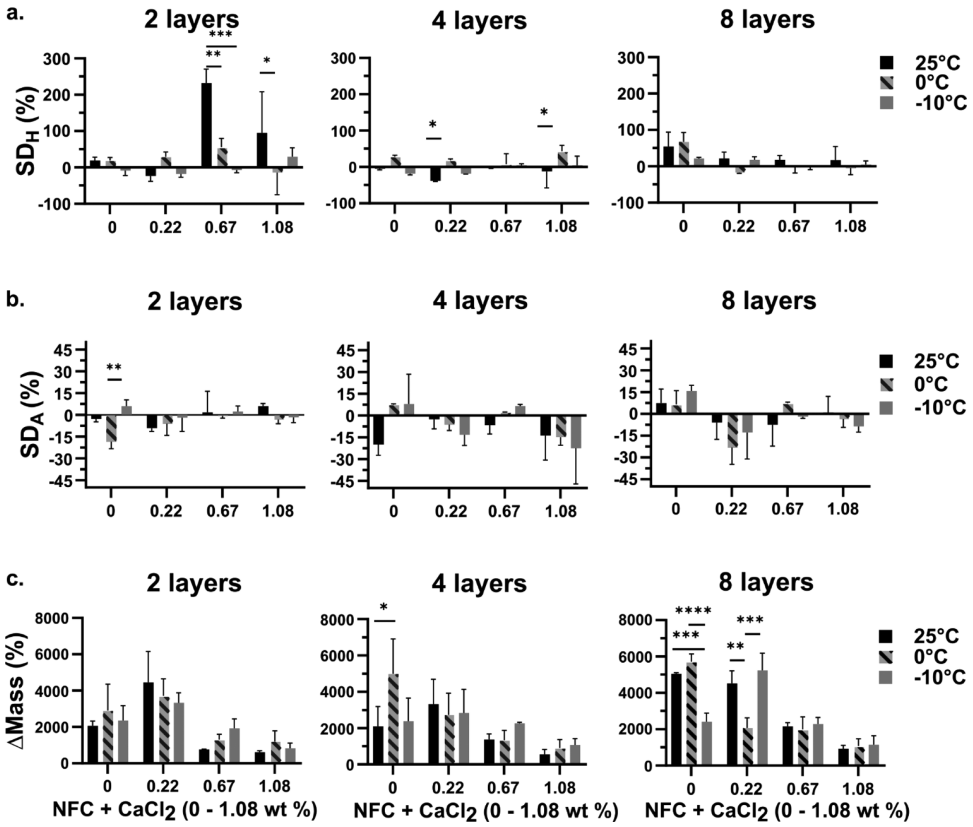

Figure 6. Effect of the cooling stage temperature and the $CaCl_2$ concentration on the swelling degree and water uptake. Graphical representation of 2, 4, and 8 layers after swelling in cell media for 24 h with respect to the freeze-dried multilayered samples for (a) percentage of the swelling degree of height SD_H (%) using eq 1, (b) percentage of the swelling degree of area SD_A (%) using eq 2, and (c) percentage of change in mass ΔMass (%) after swelling in cell media for 24 h using eq 3. Two-way Anova analysis with Tukey test was conducted for two replicas. *P*-values <0.05 are considered significant and shown on the graphs with respect to the respective sample's height of the volumetric structure printed at 25 °C. 0.0332 (**P*), 0.0021 (***P*), 0.0002 (****P*), and <0.0001 (*****P*).

was observed by two- and four-layered structure containing 0.67 and 1.08 wt %. No significant trend was visible in change of height for eight layers. Like SD_H (%), SD_A (%), in Figure 6b, the trend was also not significant. This shows that most samples maintained their shapes after swelling for 24 h.

Overall, no significant trend was visible for SD_H (%) (Figure 6a) except for 0.67 and 1.08 wt % (25 °C). Figure 6b shows that the SD_A (%) of scaffolds containing 0.22 wt % Ca decreased by less than 30%. 0.22 wt % scaffolds could absorb the most (Figure 6c) without compromising the structural dimensions and shape of the multilayered scaffold. Higher amount of $CaCl_2$ might have made the scaffolds too rigid to absorb high amount of water as the scaffolds containing 1.08 wt % $CaCl_2$ absorbed the least amount of water.

Hence, the data shown in Figures 4−6 proved that the multilayered structures made of nanocellulose with 0.22 wt % $CaCl_2$ and printed at −10 °C cold stage are the best combination for the swelling which was further proved by the biocompatibility tests.

The added $CaCl_2$ does not cause instantaneous gelation of NFC but rather enhances the printability and the ability of the printed scaffolds to maintain the desired shape. This allows the long-term storage of the NFC plus $CaCl_2$ without having to prepare a new batch each time before printing, hence eradicating any batch variations between prints ensuring repeatability. This was noticeable in the multilayered printed scaffolds with no visible difference in the printability and the structural stability of the volumetric constructs printed using the same batch over a six-month period.

3.5. Biocompatibility. To study the biocompatibility of the printed structures, adherent MEF cells were cultured on the nanocellulose scaffolds for 48 h. Cells were cultured in high concentration (100,000 cells/well) in order to observe the effect of the 3D living space provided by the scaffold, rather than the cell proliferation rate in general. As seen from the cell viability assay (Figure 7a), the cells were viable only when grown with NFC, as the culture plates used were nonadherent and could not support the growth of the cells. However, as cells plated in wells containing the NFCs extruded together with different $CaCl_2$ concentrations were compared, it was obvious that adding the $CaCl_2$ within the hydrogel increased cell viability even further, which can be observed as increased luminescence. Out of the three $CaCl_2$ concentrations used (0.22, 0.67, and 1.08 wt %), the smallest $CaCl_2$ concentration was the most optimal for the cells, when NFC was printed either in −10 °C or +25 °C (Figure 7a). Whether Ca can dissolve from the NFC during incubation is not known, and to control that, we tested how adding $CaCl_2$ straight into the growth media would affect the cell growth. We added 10 mM $CaCl_2$ (0 + Ca), which equals to 0.11 wt % of $CaCl_2$ within the NFC and observed no change in cell viability (Figure 7a), suggesting that the Ca was affecting to cell viability *via* the structure of the substrate, rather than affecting cell metabolism as a soluble ion.

https://dx.doi.org/10.1021/acsomega.0c05036
ACS Omega XXXX, XXX, XXX−XXX

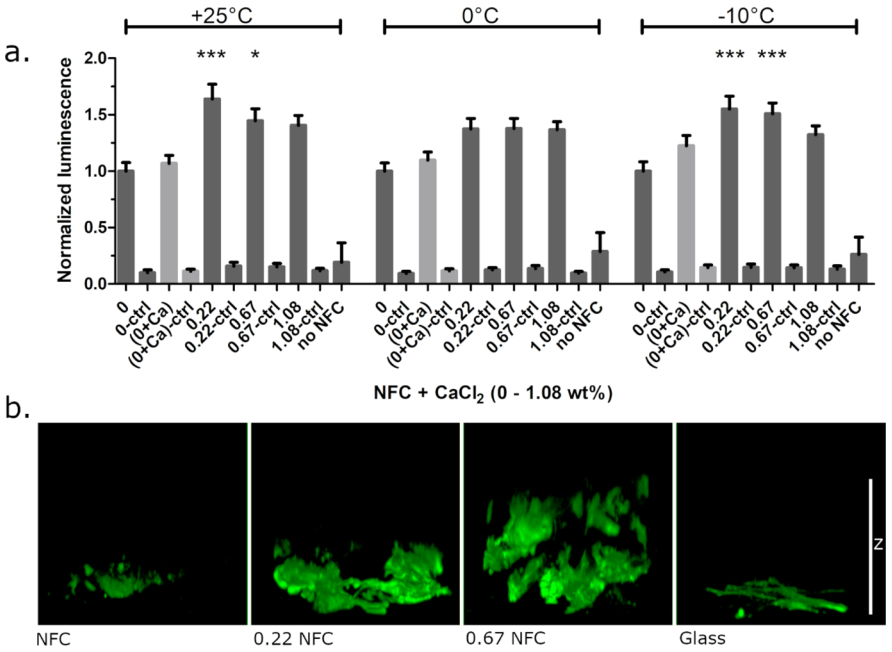

Figure 7. Cross-linking of $CaCl_2$ in nanocellulose improved cell viability. (a) Cell viability measured as the relative amount of ATP within each sample. The NFC without $CaCl_2$ cross-linking is marked as 0 and when $CaCl_2$ is added in different concentrations (wt %), samples are marked as 0.22, 0.67, and 1.08. In the 0 + $CaCl_2$ sample, 10 mM $CaCl_2$ was added to the medium. Controls (ctrl) are samples without cells. No NFC refers to the sample containing cells in culture medium without nanocellulose. Data are normalized to the NFC without $CaCl_2$ (marked as 0). The statistical significance of all results was analyzed by one-way ANOVA and Bonferroni test: $^*P < 0.05$, $^{**}P < 0.01$, and $^{***}P < 0.001$ when compared to the NFC without Ca (marked as 0). (b) 3D rendering of the *z*-stacks of the fluorescence microscopy images of the MEF cells cultured on different types of nanocellulose for 48 h. High population of MEF cells is observed in $CaCl_2$ cross-linked NFC samples. Glass coverslip (2D) was used as the control. Scale bar (Z) is 50 μm.

Our hypothesis for the addition of $CaCl_2$ was that the porosity/enhanced structure caused by the added calcium would enhance the cells' ability to reach higher into the 3D matrix of the NFC. This hypothesis was further reinforced with the notion that cell viability was increased in NFCs printed with $CaCl_2$, suggesting that cells had more space to grow into. To visualize whether the cells are able to reach higher into NFC, we transfected the cells with LifeAct-GFP that expresses an actin-binding peptide fused with green fluorescent protein leading to fluorescent actin fibers that can be monitored within live cells. We let the cells settle into the NFC for 24 h and visualized the cell morphology with a confocal microscope and obtaining z-stack images (Figures 7b and S2). As the images show, NFC without calcium shows cells on the bottom of the container, whereas with increased calcium concentration cells are able to inhabit the NFC higher in the *z*-direction, suggesting that the porosity provided by $CaCl_2$ addition improved the biocompatibility of the NFC.

4. CONCLUSIONS

The addition of the cooling stage to the bioprinter enhances the structural stability of multilayered printed structures. Although the temperature of the cooling stage did not affect the biocompatibility of the 3D structures, the addition of $CaCl_2$ had a significant impact on the structural stability of the 3D structures and hence improved the cell viability of MEF cells cultured within the scaffold. This study provides a protocol for the fabrication of stable volumetric constructs without the need for a calcium bath using *in situ* cold stage and adding $CaCl_2$ in the printing ink. This also provides the recipe for improving the biocompatibility of the scaffolds. These results can be used to fabricate precise multilayered structures which maintain their structure during cell culture for tissue regeneration and organ-on-chip applications. In addition to nanocellulose, the proposed methodology can be utilized for other printable hydrogels which do not have instantaneous gelation.

■ ASSOCIATED CONTENT

Supporting Information

The Supporting Information is available free of charge at https://pubs.acs.org/doi/10.1021/acsomega.0c05036.

Titration process of NFC 1.15 wt % to calculate the amount of the acidic group, literature review to find a suitable range of $CaCl_2$, dimensions of the hydrogel pipetted in well plates for cell culture, and maximum intensity projection of the 3D images (PDF)

■ AUTHOR INFORMATION

Corresponding Authors

Anum Rasheed − *Faculty of Medicine and Health Technology, Tampere University, 33720 Tampere, Finland;* orcid.org/0000-0001-9260-4490; Phone: +358 44 9360 767; Email: anum.rasheed@tuni.fi

Sampo Tuukkanen − *Faculty of Medicine and Health Technology, Tampere University, 33720 Tampere, Finland;* orcid.org/0000-0002-4090-7278; Phone: +358 40 541 5276; Email: sampo.tuukkanen@tuni.fi

Authors

Latifeh Azizi − *Faculty of Medicine and Health Technology, Tampere University, 33520 Tampere, Finland*

Paula Turkki − *Faculty of Medicine and Health Technology, Tampere University, 33520 Tampere, Finland*

https://dx.doi.org/10.1021/acsomega.0c05036
ACS Omega XXXX, XXX, XXX−XXX

Marika Janka − *Faculty of Medicine and Health Technology, Tampere University, 33720 Tampere, Finland*
Vesa P. Hytönen − *Faculty of Medicine and Health Technology, Tampere University, 33520 Tampere, Finland; Fimlab Laboratories, 33520 Tampere, Finland*

Complete contact information is available at: https://pubs.acs.org/10.1021/acsomega.0c05036

Author Contributions

The manuscript was written through contributions of all authors. All authors have given approval to the final version of the manuscript.

Funding

Research funding for A.R. is provided by the graduate school of Tampere University. L.A. received support from the graduate school of Tampere University.

Notes

The authors declare no competing financial interest.

■ ACKNOWLEDGMENTS

We acknowledge the research funding provided by the graduate school of Tampere University. We also acknowledge Orlando J. Rojas, Aalto University, Finland, for providing the nanocellulose used in this study. Furthermore, we would like to acknowledge the Biocenter Finland for infrastructure support and Academy of Finland for the financial support (grant no. 290506). The authors also acknowledge the insightful opinions provided by Professor Minna Kellomäki to enhance the manuscript in its final stages.

■ ABBREVIATIONS

NFC, nanofibrillated cellulose; CAD, computer-aided design; DXF, drawing eXchange format; MEF cells, mouse embryonic fibroblast cells; RH, relative humidity

■ REFERENCES

(1) Miri, A. K.; Mirzaee, I.; Hassan, S.; Mesbah Oskui, S.; Nieto, D.; Khademhosseini, A.; Zhang, Y. S. Effective Bioprinting Resolution in Tissue Model Fabrication. *Lab Chip* **2019**, *19*, 2019−2037.
(2) Foster, A. J.; Chouhan, B.; Regan, S. L.; Rollison, H.; Amberntsson, S.; Andersson, L. C.; Srivastava, A.; Darnell, M.; Cairns, J.; Lazic, S. E.; Jang, K.-J.; Petropolis, D. B.; Kodella, K.; Rubins, J. E.; Williams, D.; Hamilton, G. A.; Ewart, L.; Morgan, P. Integrated in Vitro Models for Hepatic Safety and Metabolism: Evaluation of a Human Liver-Chip and Liver Spheroid. *Arch. Toxicol.* **2019**, *93*, 1021−1037.
(3) Jiang, J.; Pieterman, C. D.; Ertaylan, G.; Peeters, R. L. M.; de Kok, T. M. C. M. The Application of Omics-Based Human Liver Platforms for Investigating the Mechanism of Drug-Induced Hepatotoxicity in Vitro. *Arch. Toxicol.* **2019**, *93*, 3067−3098.
(4) He, Y.; Xie, M.; Gao, Q.; Fu, J. Why Choose 3D Bioprinting? Part I: A Brief Introduction of 3D Bioprinting for the Beginners. *Bio-Des. Manuf.* **2019**, *2*, 221−224.
(5) Idaszek, J.; Costantini, M.; Karlsen, T. A.; Jaroszewicz, J.; Colosi, C.; Testa, S.; Fornetti, E.; Bernardini, S.; Seta, M.; Kasarełło, K.; Wrzesień, R.; Cannata, S.; Barbetta, A.; Gargioli, C.; Brinchman, J. E.; Święszkowski, W. 3D Bioprinting of Hydrogel Constructs with Cell and Material Gradients for the Regeneration of Full-Thickness Chondral Defect Using a Microfluidic Printing Head. *Biofabrication* **2019**, *11*, DOI: 10.1088/1758-5090/ab2622.
(6) Yu, F.; Choudhury, D. Microfluidic Bioprinting for Organ-on-a-Chip Models. *Drug Discov. Today* **2019**, *24*, 1248−1257.
(7) Fetah, K.; Tebon, P.; Goudie, M. J.; Eichenbaum, J.; Ren, L.; Barros, N.; Nasiri, R.; Ahadian, S.; Ashammakhi, N.; Dokmeci, M. R.; Khademhosseini, A. The Emergence of 3D Bioprinting in Organ-on-Chip Systems. *Prog. Biomed. Eng.* **2019**, *1*, 012001.
(8) Abudupataer, M.; Chen, N.; Yan, S.; Alam, F.; Shi, Y.; Wang, L.; Lai, H.; Li, J.; Zhu, K.; Wang, C. Bioprinting a 3D Vascular Construct for Engineering a Vessel-on-a-Chip. *Biomed. Microdevices* **2020**, *22*, 1−10.
(9) Malda, J.; Visser, J.; Melchels, F. P.; Jüngst, T.; Hennink, W. E.; Dhert, W. J. A.; Groll, J.; Hutmacher, D. W. 25th Anniversary Article: Engineering Hydrogels for Biofabrication. *Adv. Mater.* **2013**, *25*, 5011−5028.
(10) Kilian, D.; Ahlfeld, T.; Akkineni, A. R.; Lode, A.; Gelinsky, M. Three-Dimensional Bioprinting of Volumetric Tissues and Organs. *MRS Bull.* **2017**, *42*, 585−592.
(11) Kundu, J.; Pati, F.; Hun Jeong, Y.; Cho, D. W. Biomaterials for Biofabrication of 3D Tissue Scaffolds. *Biofabrication: Micro- and Nano-fabrication, Printing, Patterning and Assemblies*; Elsevier Inc., 2013; pp 23−46.
(12) Murphy, S. V.; Atala, A. 3D Bioprinting of Tissues and Organs. *Nat. Biotechnol.* **2014**, *32*, 773−785.
(13) Yamada, K. M.; Sixt, M. Mechanisms of 3D Cell Migration. *Nat. Rev. Mol. Cell Biol.* **2019**, *20*, 738−752.
(14) Brevini, T. A. L.; Pennarossa, G.; Gandolfi, F. A 3D Approach to Reproduction. *Theriogenology* **2020**, *150*, 2−7.
(15) Fontoura, J. C.; Viezzer, C.; dos Santos, F. G.; Ligabue, R. A.; Weinlich, R.; Puga, R. D.; Antonow, D.; Severino, P.; Bonorino, C. Comparison of 2D and 3D Cell Culture Models for Cell Growth, Gene Expression and Drug Resistance. *Mater. Sci. Eng. C* **2020**, *107*, 110264.
(16) Gaut, L.; Bonnin, M.-A.; Blavet, C.; Cacciapuoti, I.; Orpel, M.; Mericskay, M.; Duprez, D. Mechanical and Molecular Parameters That Influence the Tendon Differentiation Potential of C3H10T1/2 Cells in 2D- And 3D-Culture Systems. *Biol. Open* **2020**, *9*, DOI: 10.1242/bio.047928.
(17) Jung, J. P.; Bhuiyan, D. B.; Ogle, B. M. Solid Organ Fabrication: Comparison of Decellularization to 3D Bioprinting. *Biomater. Res.* **2016**, *20*, 1−11.
(18) Ma, X.; Qu, X.; Zhu, W.; Li, Y.-S.; Yuan, S.; Zhang, H.; Liu, J.; Wang, P.; Lai, C. S. E.; Zanella, F.; Feng, G.-S.; Sheikh, F.; Chien, S.; Chen, S. Deterministically Patterned Biomimetic Human IPSC-Derived Hepatic Model via Rapid 3D Bioprinting. *Proc. Natl. Acad. Sci. U.S.A.* **2016**, *113*, 2206−2211.
(19) Wang, R.; Wang, Y.; Yao, B.; Hu, T.; Li, Z.; Huang, S.; Fu, X. Beyond 2D: 3D Bioprinting for Skin Regeneration. *Int. Wound J.* **2019**, *16*, 134−138.
(20) Wang, X.; Wang, Q.; Xu, C. Nanocellulose-Based Inks for 3D Bioprinting: Key Aspects in Research Development and Challenging Perspectives in Applications-A Mini Review. *Bioengineering* **2020**, *7*, 40.
(21) Vermeulen, N.; Haddow, G.; Seymour, T.; Faulkner-Jones, A.; Shu, W. 3D Bioprint Me: A Socioethical View of Bioprinting Human Organs and Tissues. *J. Med. Ethics* **2017**, *43*, 618−624.
(22) Ozbolat, I. T.; Yin Yu, Y. Bioprinting toward Organ Fabrication: Challenges and Future Trends. *IEEE Trans. Biomed. Eng.* **2013**, *60*, 691−699.
(23) Guillotin, B.; Ali, M.; Ducom, A.; Catros, S.; Keriquel, V.; Souquet, A.; Remy, M.; Fricain, J. C.; Guillemot, F. Laser-Assisted Bioprinting for Tissue Engineering. *Biofabrication: Micro- and Nano-fabrication, Printing, Patterning and Assemblies*; Elsevier Inc., 2013; pp 95−118.
(24) Bishop, E. S.; Mostafa, S.; Pakvasa, M.; Luu, H. H.; Lee, M. J.; Wolf, J. M.; Ameer, G. A.; He, T. C.; Reid, R. R. 3-D Bioprinting Technologies in Tissue Engineering and Regenerative Medicine: Current and Future Trends. *Genes Dis.* **2017**, *4*, 185−195.
(25) Chang, C. C.; Boland, E. D.; Williams, S. K.; Hoying, J. B. Direct-Write Bioprinting Three-Dimensional Biohybrid Systems for Future Regenerative Therapies. *J. Biomed. Mater. Res., Part B* **2011**, *98B*, 160−170.

(26) Huan, S.; Ajdary, R.; Bai, L.; Klar, V.; Rojas, O. J. Low Solids Emulsion Gels Based on Nanocellulose for 3D-Printing. *Biomacromolecules* **2019**, *20*, 635−644.
(27) Lin, F.; Zheng, R.; Chen, J.; Su, W.; Dong, B.; Lin, C.; Huang, B.; Lu, B. Microfibrillated Cellulose Enhancement to Mechanical and Conductive Properties of Biocompatible Hydrogels. *Carbohydr. Polym.* **2019**, *205*, 244−254.
(28) Heggset, E. B.; Strand, B. L.; Sundby, K. W.; Simon, S.; Chinga-Carrasco, G.; Syverud, K. Viscoelastic Properties of Nanocellulose Based Inks for 3D Printing and Mechanical Properties of CNF/Alginate Biocomposite Gels. *Cellulose* **2019**, *26*, 581−595.
(29) Naseri, N.; Deepa, B.; Mathew, A. P.; Oksman, K.; Girandon, L. Nanocellulose-Based Interpenetrating Polymer Network (IPN) Hydrogels for Cartilage Applications. *Biomacromolecules* **2016**, *17*, 3714−3723.
(30) Martínez Ávila, H.; Schwarz, S.; Rotter, N.; Gatenholm, P. 3D Bioprinting of Human Chondrocyte-Laden Nanocellulose Hydrogels for Patient-Specific Auricular Cartilage Regeneration. *Bioprinting* **2016**, *1*−*2*, 22−35.
(31) Krontiras, P.; Gatenholm, P.; Hägg, D. A. Adipogenic Differentiation of Stem Cells in Three-Dimensional Porous Bacterial Nanocellulose Scaffolds. *J. Biomed. Mater. Res., Part B* **2015**, *103*, 195−203.
(32) Markstedt, K.; Mantas, A.; Tournier, I.; Martínez Ávila, H.; Hägg, D.; Gatenholm, P. 3D Bioprinting Human Chondrocytes with Nanocellulose-Alginate Bioink for Cartilage Tissue Engineering Applications. *Biomacromolecules* **2015**, *16*, 1489−1496.
(33) Rees, A.; Powell, L. C.; Chinga-Carrasco, G.; Gethin, D. T.; Syverud, K.; Hill, K. E.; Thomas, D. W. 3D Bioprinting of Carboxymethylated-Periodate Oxidized Nanocellulose Constructs for Wound Dressing Applications. *Biomed Res. Int.* **2015**, *2015*, 925757.
(34) Leppiniemi, J.; Lahtinen, P.; Paajanen, A.; Mahlberg, R.; Metsä-Kortelainen, S.; Pinomaa, T.; Pajari, H.; Vikholm-Lundin, I.; Pursula, P.; Hytönen, V. P. 3D-Printable Bioactivated Nanocellulose-Alginate Hydrogels. *ACS Appl. Mater. Interfaces* **2017**, *9*, 21959−21970.
(35) Ribeiro, A.; Blokzijl, M. M.; Levato, R.; Visser, C. W.; Castilho, M.; Hennink, W. E.; Vermonden, T.; Malda, J. Assessing Bioink Shape Fidelity to Aid Material Development in 3D Bioprinting. *Biofabrication* **2017**, *10*, 014102.
(36) Park, S.; Kim, S.; Choi, J. Development of a Multi-Nozzle Bioprinting System for 3D Tissue Structure Fabrication. *ICCAS 2015—2015 15th International Conference on Control, Automation and Systems, Proceedings*; IEEE, 2015; pp 1874−1877.
(37) Guo, J.; Filpponen, I.; Su, P.; Laine, J.; Rojas, O. J. Attachment of Gold Nanoparticles on Cellulose Nanofibrils via Click Reactions and Electrostatic Interactions. *Cellulose* **2016**, *23*, 3065−3075.
(38) Liu, W.; Zhang, Y. S.; Heinrich, M. A.; De Ferrari, F.; Jang, H. L.; Bakht, S. M.; Alvarez, M. M.; Yang, J.; Li, Y.-C.; Trujillo-de Santiago, G.; Miri, A. K.; Zhu, K.; Khoshakhlagh, P.; Prakash, G.; Cheng, H.; Guan, X.; Zhong, Z.; Ju, J.; Zhu, G. H.; Jin, X.; Shin, S. R.; Dokmeci, M. R.; Khademhosseini, A. Bioprinting: Rapid Continuous Multimaterial Extrusion Bioprinting (Adv. Mater. 3/2017). *Adv. Mater.* **2017**, *29*, DOI: 10.1002/adma.201770016.
(39) Lee, J. M.; Sing, S. L.; Yeong, W. Y. Bioprinting of Multimaterials with Computer-aided Design/Computer -aided Manufacturing. *Int. J. Bioprint.* **2020**, *6*, 65−73.
(40) Goh, G. D.; Yap, Y. L.; Tan, H. K. J.; Sing, S. L.; Goh, G. L.; Yeong, W. Y. Process−Structure−Properties in Polymer Additive Manufacturing via Material Extrusion: A Review. *Critical Reviews in Solid State and Materials Sciences*; Taylor and Francis Inc., 2020, pp 113−133.
(41) Berk, Z. Freeze Drying (Lyophilization) and Freeze Concentration. In *Food Process Engineering and Technology*; Berk, Z., Ed.; Food Science and Technology; Academic Press: San Diego, 2013; pp 567−581.
(42) Liu, J.; Chinga-Carrasco, G.; Cheng, F.; Xu, W.; Willför, S.; Syverud, K.; Xu, C. Hemicellulose-Reinforced Nanocellulose Hydrogels for Wound Healing Application. *Cellulose* **2016**, *23*, 3129−3143.
(43) Yang, Y.; Lu, Y.-T.; Zeng, K.; Heinze, T.; Groth, T.; Zhang, K. Recent Progress on Cellulose-Based Ionic Compounds for Biomaterials. *Adv. Mater.* **2020**, 2000717.
(44) Mertaniemi, H.; Escobedo-Lucea, C.; Sanz-Garcia, A.; Gandía, C.; Mäkitie, A.; Partanen, J.; Ikkala, O.; Yliperttula, M. Human Stem Cell Decorated Nanocellulose Threads for Biomedical Applications. *Biomaterials* **2016**, *82*, 208−220.
(45) Alexandrescu, L.; Syverud, K.; Gatti, A.; Chinga-Carrasco, G. Cytotoxicity Tests of Cellulose Nanofibril-Based Structures. *Cellulose* **2013**, *20*, 1765−1775.
(46) Rajala, S.; Siponkoski, T.; Sarlin, E.; Mettänen, M.; Vuoriluoto, M.; Pammo, A.; Juuti, J.; Rojas, O. J.; Franssila, S.; Tuukkanen, S. Cellulose Nanofibril Film as a Piezoelectric Sensor Material. *ACS Appl. Mater. Interfaces* **2016**, *8*, 15607−15614.
(47) Xu, C.; Zhang Molino, B.; Wang, X.; Cheng, F.; Xu, W.; Molino, P.; Bacher, M.; Su, D.; Rosenau, T.; Willför, S.; Wallace, G. 3D Printing of Nanocellulose Hydrogel Scaffolds with Tunable Mechanical Strength towards Wound Healing Application. *J. Mater. Chem. B* **2018**, *6*, 7066−7075.
(48) Kiiskinen, J.; Merivaara, A.; Hakkarainen, T.; Kääriäinen, M.; Miettinen, S.; Yliperttula, M.; Koivuniemi, R. Nanofibrillar Cellulose Wound Dressing Supports the Growth and Characteristics of Human Mesenchymal Stem/Stromal Cells without Cell Adhesion Coatings. *Stem Cell Res. Ther.* **2019**, *10*, 1−13.
(49) Curvello, R.; Raghuwanshi, V. S.; Garnier, G. Engineering Nanocellulose Hydrogels for Biomedical Applications. *Adv. Colloid Interface Sci.* **2019**, *267*, 47−61.
(50) Bhattacharya, M.; Malinen, M. M.; Lauren, P.; Lou, Y.-R.; Kuisma, S. W.; Kanninen, L.; Lille, M.; Corlu, A.; GuGuen-Guillouzo, C.; Ikkala, O.; Laukkanen, A.; Urtti, A.; Yliperttula, M. Nanofibrillar Cellulose Hydrogel Promotes Three-Dimensional Liver Cell Culture. *J. Controlled Release* **2012**, *164*, 291−298.

https://dx.doi.org/10.1021/acsomega.0c05036
ACS Omega XXXX, XXX, XXX−XXX